Journal of Applied Physics

RESEARCH ARTICLE | APRIL 07 2022

Refractive index dispersion of BGa(As)P alloys in the near-infrared for III-V laser integration on silicon

Christopher R. Fitch; Dominic A. Duffy; Peter Ludewig; ... et. al

Journal of Applied Physics 131, 133102 (2022)
https://doi.org/10.1063/5.0081069

AIP Publishing

Journal of Applied Physics ARTICLE scitation.org/journal/jap

Refractive index dispersion of BGa(As)P alloys in the near-infrared for III-V laser integration on silicon

Cite as: J. Appl. Phys. **131**, 133102 (2022); doi: 10.1063/5.0081069
Submitted: 6 December 2021 · Accepted: 22 March 2022 ·
Published Online: 7 April 2022

Christopher R. Fitch,[1] Dominic A. Duffy,[1] Peter Ludewig,[2] Wolfgang Stolz,[2,3] and Stephen J. Sweeney[1,a)]

AFFILIATIONS

[1]Advanced Technology Institute and Department of Physics, University of Surrey, Guildford, GU2 7XH, United Kingdom
[2]NAsP III/V GmbH, Am Knechtacker 19, 35041, Marburg, Germany
[3]Material Sciences Center and Department of Physics, Philipps-Universität, Hans-Meerwein-Strasse, 35032, Marburg, Germany

[a)]**Author to whom correspondence should be addressed:** s.sweeney@surrey.ac.uk

ABSTRACT

$B_xGa_{(1-x)}P$ and $B_xGa_{(1-x)}As_yP_{(1-y)}$ alloys are of potential interest in III-V heterostructures for integration with silicon. Waveguide design utilizing these alloys requires an understanding of the refractive index properties and their variation with composition. Refractive index dispersion was measured and modeled in the wavelength range of 827–2254 nm using spectroscopic ellipsometry at room temperature for samples with boron and arsenic fractions from 0% to 6.6% and 0% to 17%, respectively. The refractive index was found to increase with increasing boron composition as a result of strain due to lattice constant mismatch with the silicon substrate. For the arsenic-containing alloy, the refractive index was found to increase independently of strain. An empirical model based on the composition dependent variation of Cauchy dispersion function coefficients was developed for BGaAsP alloys lattice matched to silicon at the growth temperature. This model can be used to calculate the wavelength dependent refractive index of lattice matched boron and arsenic combinations for applications in semiconductor waveguides, an example of which is proposed. The results of this study are of interest more broadly for other III-V on silicon applications including photovoltaics and more generally in terms of the ellipsometric investigations of thin films on non-native substrates.

I. INTRODUCTION

Silicon photonic device research and development continues to be motivated by growth in data and telecoms traffic, the need to reduce power consumption in data centers and opportunities for low cost, high density, large scale commercial manufacture by the established complementary metal oxide semiconductor (CMOS) industry. Integration of photonics and conventional electronics provides a range of benefits including smaller physical size, higher speed, and lower power consumption.

Important building blocks for photonic integration including multiplexers, high-speed modulators, low-loss waveguides, and photodetectors are now available[1] and optical interconnect solutions are being used in data centers. However, a key requirement for ongoing implementation is an electrically pumped, temperature stable on-chip silicon-based laser operating above room temperature (RT) and compatible with existing CMOS processing procedures and infrastructure.[2,3]

Silicon is an indirect bandgap semiconductor and consequently poor for light emission. While approaches to develop an all-silicon laser continue to be investigated, they are currently technically complex and less suitable for low cost, high volume, and high consistency mass production. On the other hand, direct bandgap III-V materials have been studied and optimized as gain media for decades resulting in the establishment of efficient lasers using a range of materials, e.g., indium phosphide and gallium arsenide based alloys, and integration of III-V semiconductors on a silicon substrate is currently the most practical way of achieving on-chip light sources for silicon photonics. The two main integration approaches are wafer bonding-based heterogeneous integration

of a III-V epitaxial layer on silicon circuits and direct monolithic epitaxial growth. The large number of lasers required for applications such as on-chip interconnects economically favor a monolithic integration approach.

However, there are a number of technical difficulties associated with the monolithic integration of III-Vs onto silicon:

- Lattice constant mismatch between III-V materials and silicon—leading to threading dislocations.
- Thermal expansion coefficient mismatch—leading to micro-thermal cracks.
- Polar/non-polar interfaces—leading to the formation of anti-phase domains (APDs).[4]

All of these impact device performance and lifetime. These issues and the stringent requirements of CMOS compatibility (e.g., processing temperature <450 °C) make the realization of monolithic solutions challenging. The materials adopted by the telecommunications industry based on GaAs and InP, which may be readily exploited through hybrid integration, cannot be directly heteroepitaxially deposited on silicon without the development of crystal defects and the possibility of macroscopic cracking.

The lattice constant of silicon (5.4311 Å at 299 K[5]) is smaller than that of GaP (5.4505 Å at 300 K[6]) which is the smallest of the natural zincblende III-V alloys. A GaP nucleation layer free from dislocations, stacking faults, twins, and antiphase disorder can be grown on a silicon homoepitaxial buffer by metal organic vapor phase epitaxy (MOVPE)[7,8] to form a GaP/Si virtual substrate. Unfortunately, GaP is also an indirect semiconductor and unsuitable as a laser gain medium itself; however, the addition of arsenic to form GaAsP produces a direct bandgap material although this increases the lattice constant mismatch to silicon. By alloying GaP with a small fraction of nitrogen (<10%) and a large fraction of arsenic (>70%) the dilute nitride quaternary GaNAsP is formed which has a direct bandgap and closely matches the lattice constant of GaP and silicon[9] thus avoiding the formation of misfit and threading dislocations.

Electrically injected GaNAsP quantum well (QW) lasers operating at 981 nm have been realized on GaP substrates at room temperature[10–12] with a threshold current density (J_{th}) of 4.0 kA cm^{-2} and characteristic temperature (T_0) of 58 K (220–295 K). Lasing operation has also been achieved up to 165 K at 860 nm on a GaP/Si substrate[13–15] with a J_{th} of 1.6 kA cm^{-2} and a T_0 of 73 K (100–165 K). These threshold current densities are significantly higher than more established GaAs-based lasers which operate at similar wavelengths with J_{th}/QW ~ 100–200 A cm^{-2}. Improvements in laser device characteristics are expected to be achieved through a combination of optimization of the growth conditions for the barrier and SCH materials and the improvement of the electrical and optical confinement.

In the ongoing development of these lasers, p- or n-doped BGaP is used for cladding and BGaAsP for the separate confinement heterostructure (SCH) layers. The relatively thick layers also provide strain compensation for the compressively strained QW material. Figure 1 shows a schematic representation of a GaNAsP QW laser structure, which provides the context for our investigation.

In order to limit the formation of threading dislocations, the device layers need to be lattice matched to the silicon substrate at the growth temperature. Lattice matching of BGaP to silicon is achieved at ~3% boron at a growth temperature of 575 °C, while for the BGaAsP SCH layers, lattice matching is maintained by offsetting an increased boron fraction by the addition of arsenic. An important consideration in this work is that when cooled to RT these III-V layers become tensile strained relative to the substrate.

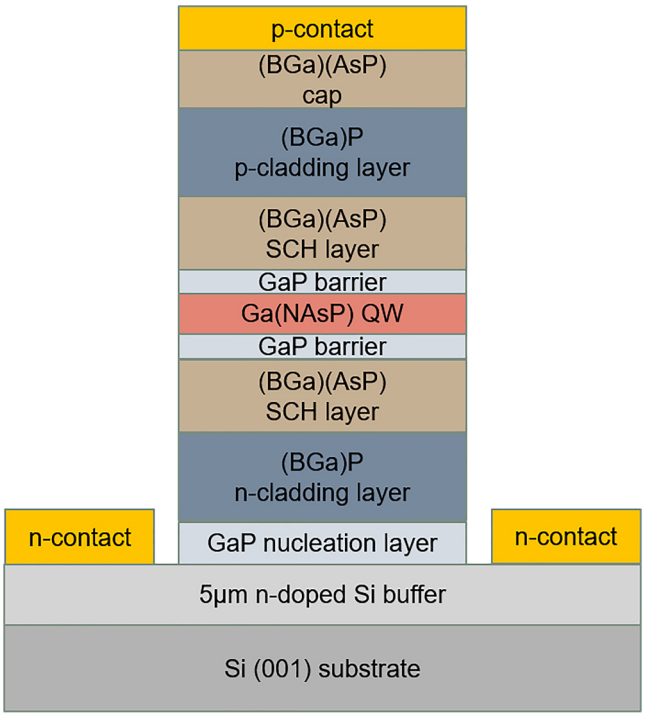

FIG. 1. Schematic representation of a GaNAsP QW laser device showing substrate, cladding, SCH, and barrier layers.

Figure 2 shows how the relaxed lattice constant of the BGa(As)P alloy at RT varies as a function of boron and arsenic fraction with respect to the silicon substrate. This illustrates how adding boron to GaP can reduce its lattice constant to match that of silicon and that at RT, $B_{3\%}Ga_{97\%}P$ deposited on silicon would be under tensile strain as its relaxed lattice constant is less than that of silicon. The figure also shows that the addition of arsenic can be used to balance further increases in boron fraction to maintain lattice matching to silicon.

Lattice matching to minimize defect density is one approach to improving device performance. However, the stimulated emission process is also dependent on the photon density within the laser cavity, and a moderate increase in the optical confinement factor can give rise to significant improvements in modal gain and hence in device performance. Maximizing the confinement factor requires that the core (the quantum well and barriers) and cladding provide a good waveguide. The strength of the light coupling into the waveguide is dependent on the difference in the refractive index between the core and the cladding (the contrast) and the thickness of the active region.

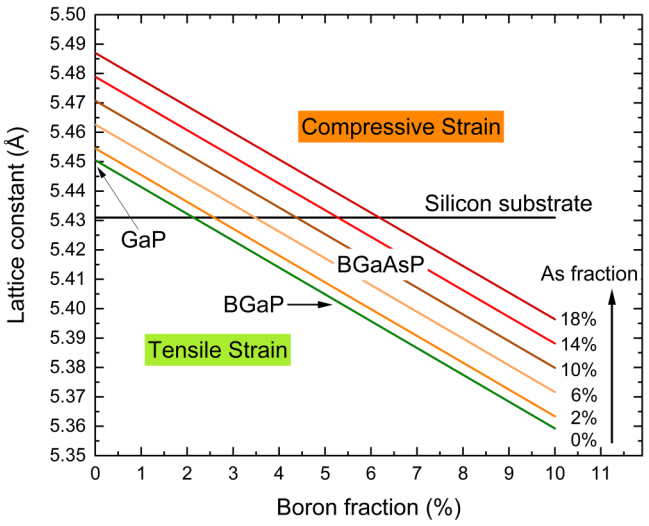

FIG. 2. Variation in relaxed lattice constant of BGa(As)P alloys with boron and arsenic fraction at room temperature relative to silicon.

Design of the waveguide and carrier confinement components of these devices therefore requires an understanding of the optical and electronic properties of the $B_xGa_{(1-x)}P$ and $B_xGa_{(1-x)}As_yP_{(1-y)}$ materials and their variation with composition. Previous investigations of the refractive index have been carried out by Rogowsky *et al.*[16] and Volk and Stolz[17] and the bandgap properties have been investigated by Hossain *et al.*[18] However, these do not cover the full wavelength range of interest, from 850 to 1300 nm (1.46–0.95 eV), which may be achieved by bandgap engineering (varying the composition and strain) of the GaNAsP system.

As well as the boron containing alloys, we are also interested in determining the refractive index of the compressively strained GaP nucleation layers and the doped silicon substrates. Refractive index is sensitive to strain, doping, and differences in crystalline quality and impurities, which may be associated with different deposition methods. With ongoing improvements in deposition technology and processes, it is important to use measured values, which are specific to the deposition system deployed rather than relying on literature data even for the more commonly documented materials. The refractive index of the GaNAsP QW has not been measured in this study but from other studies[19–21] can be assumed to be >3.3 for the wavelength range considered here.

The methodology and results of this study are also relevant to other applications using similar material systems. For example, BGaAs/GaP QWs grown on a GaP/Si virtual substrates are being investigated as promising optical gain media for red-light emitters.[22–24] Furthermore, dilute nitride and phosphide materials including GaNPAs and GaNP[25] and GaAsP[26] are being investigated as candidates for integration of photovoltaics on silicon. The approach of lattice matching to silicon by alloying with smaller atoms is common in photovoltaics, for example, adding small amounts of boron to GaInAs.[27]

Spectroscopic ellipsometry (SE) provides a method for very precise measurement of a range of material properties including refractive index. The optical properties of the $B_xGa_{(1-x)}P$, $B_xGa_{(1-x)}As_yP_{(1-y)}$, GaP, and silicon materials are measured and analyzed across the full spectral range of the ellipsometer. We report here on the detailed measurement and modeling of the real part of the refractive index, in the transparent region below the bandgap, for these materials and its variation with alloy composition and wavelength taking into consideration the substrate induced strain.

II. SAMPLES

A series of three sets of samples were produced to determine the refractive indices of the alloys using SE. A summary of the characteristics of each sample is given in Table I. Boron fractions were in the range of 0%–6.6% and arsenic fractions from 0%–17%.

Series 1 and 2 samples were deposited on exactly oriented silicon (001) (±0.5°) substrates with an additional 5 μm layer of highly n-doped silicon (1×10^{19} cm^{-3} P for series 1, 3×10^{19} cm^{-3} P for series 2) deposited before III-V growth. A 28 nm thick pseudomorphically strained GaP nucleation layer was deposited in a close-coupled showerhead (CCS) Crius R300 mm system on the silicon substrates. The wafers were then cleaved into smaller pieces for the deposition of BGaP and BGaAsP layers, which were grown by metal organic vapor phase epitaxy (MOVPE) in a horizontal AIX 200-GFR reactor system at 575 °C. A further 4 nm of GaP was added to the template layer before the deposition of the BGaP and BGaAsP layers.

A number of the series 1 and 2 samples were grown lattice matched to silicon at the growth temperature. The relationship between the boron (x) and arsenic (y) fractions for lattice matching at the growth temperature for these samples is illustrated in Fig. 3.

Series 3 samples were grown on GaP substrates with the BGa(As)P layers deposited directly onto the GaP substrate as described above.

All boron containing and GaP layers were nominally undoped. The BGa(As)P layers formed the topmost layer in all cases. The reverse sides of the substrates were roughened using a fine emery paper until uniformly matt to eliminate backreflection from the substrate to air interface during ellipsometry. Samples were typically rectangular with ~5–10 mm sides allowing simple ellipsometer mounting. The silicon substrate samples A and G were prepared by etching the GaP layers from the GaP on silicon templates (B and H) using aqua regia.

Layer thicknesses and alloy compositions for each of the samples were determined by dynamic model fitting of high resolution x-ray diffraction (HR-XRD) scan data using the X'Pert PRO system from PANalytical. For the BGaP samples, the uncertainty in the boron fraction from the HR-XRD simulation is ±0.05%, and for the BGaAsP samples, the boron and arsenic fraction uncertainties are ±0.1% and ±0.2%, respectively. The GaP, BGaP and BGaAsP layer thicknesses were also measured as part of the SE investigation and were confirmed to be within <5% of the HR-XRD values quoted in Table I. Critical thickness values (h_c) were calculated at 300 K after Zhang[28] and all sample layer thicknesses, with the exception of sample C, were determined to be less than h_c. Sample C (boron fraction 3.1%) has a similar boron fraction to

TABLE I. Summary of sample characteristics.

Sample	Material	Substrate	B fraction x (%)	As fraction y (%)	Thickness (nm)	h_c (300 K) (nm)	In-plane strain (300 K)
Series 1							
A	Si (n-doped)	Si	N/A	N/A	5000[a]	N/A	None
B	GaP	Si (A)	0	0	28[a]	126[b]	Compressive
C	$B_xGa_{(1-x)}P$	GaP/Si	3.1[c]	0	422[c]	359[b]	Tensile
D	$B_xGa_{(1-x)}As_yP_{(1-y)}$	GaP/Si	4.2[c]	6.0[c]	425[c]	519[b]	Tensile
E	$B_xGa_{(1-x)}As_yP_{(1-y)}$	GaP/Si	5.4[c]	12.0[c]	425[c]	694[b]	Tensile
F	$B_xGa_{(1-x)}As_yP_{(1-y)}$	GaP/Si	6.6[c]	17.0[c]	465[c]	603[b]	Tensile
Series 2							
G	Si (n-doped)	Si	N/A	N/A	5000[a]	N/A	None
H	GaP	Si (G)	0	0	28[a]	126[b]	Compressive
I	$B_xGa_{(1-x)}P$	GaP/Si	1.4[c]	0	105[c]	502[b]	Compressive
J	$B_xGa_{(1-x)}P$	GaP/Si	2.6[c]	0	105[c]	894[b]	Tensile
K	$B_xGa_{(1-x)}P$	GaP/Si	3.2[c]	0	106[c]	316[b]	Tensile
L	$B_xGa_{(1-x)}P$	GaP/Si	4.3[c]	0	104[c]	123[b]	Tensile
M	$B_xGa_{(1-x)}As_yP_{(1-y)}$	GaP/Si	4.9[c]	7.1[c]	106[c]	280[b]	Tensile
N	$B_xGa_{(1-x)}As_yP_{(1-y)}$	GaP/Si	5.0[c]	10.4[c]	108[c]	758[b]	Tensile
Series 3							
O	GaP	GaP	0	0	…	N/A	None
P	$B_xGa_{(1-x)}P$	GaP	0.42[c]	0	500[c]	1009[b]	Tensile
Q	$B_xGa_{(1-x)}P$	GaP	0.7[c]	0	500[c]	539[b]	Tensile
R	$B_xGa_{(1-x)}As_yP_{(1-y)}$	GaP	1.9[c]	6.0[c]	295[c]	925[b]	Tensile
S	$B_xGa_{(1-x)}As_yP_{(1-y)}$	GaP	2.1[c]	6.0[c]	293[c]	884[b]	Tensile
T	$B_xGa_{(1-x)}As_yP_{(1-y)}$	GaP	2.9[c]	12.0[c]	296[c]	1281[b]	Tensile

Measurement method:
[a]Nominal.
[b]Calculated.
[c]HR-XRD.

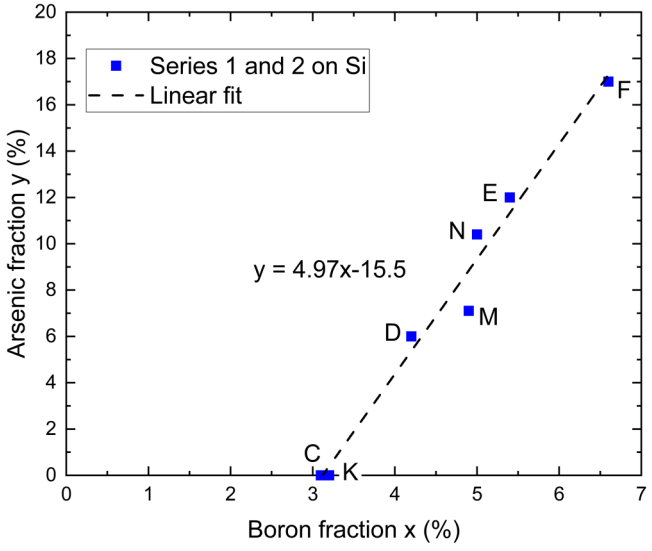

FIG. 3. Relationship between boron and arsenic fractions for lattice matching of BGaAsP at the growth temperature of 575 °C.

sample K (3.2%) allowing comparison to evaluate any differences due to relaxation. The critical thickness at the growth temperature of 575 °C is increased for layers under tensile strain and decreased for those under compressive strain. BGaP and BGaAsP layers designed to be lattice matched to silicon at the growth temperature can be grown to a thickness of more than 1.5 μm without relaxation.[29] For the GaP on silicon substrate, under compressive strain, the critical thickness is reduced at the growth temperature with the first signs of relaxation occurring at a thickness of around 70 nm.[8,29] All of the samples are, therefore, within the critical thickness at the growth temperature.

III. SPECTROSCOPIC ELLIPSOMETRY

SE is a highly sensitive, non-destructive measurement technique that can be used to determine the thickness and optical properties of thin films. SE measures the relative change in the polarization state of the p- and s-components of the electric field of the incident and, elliptically polarized, reflected light from the sample. The incident polarization state is known and the reflected polarization state is analyzed by a rotating polarizer and detector. The change in amplitude and phase of the p- and s- waves caused by reflection from the sample are characterized by the measured ellipsometric parameters

ψ and Δ, which are typically expressed in terms of the ratio of the complex reflection coefficients R_P and R_S as

$$\rho = \frac{R_P}{R_S} = \tan(\psi)e^{i\Delta} \quad (1)$$

SE does not measure layer thicknesses or optical constants directly. Instead, it relies on the development of a physically based model in which the unknown properties are varied iteratively in order to achieve the best possible fit between the modeled and experimentally measured data. A Levenberg–Marquardt regression fitting algorithm is used to reduce the mean square error (MSE) between the model calculated and the measured ψ and Δ data sets by adjusting the model parameters.[30] The parametric model is described in Sec. IV.

IV. EXPERIMENTAL APPROACH

SE data were collected using a variable angle spectroscopic ellipsometer (J. A. Woollam V-VASE) with an extended wavelength range (250–2500 nm) HS-190™ scanning double monochromator and 75 W xenon light source. The data analyzed for refractive index investigation were in the range of 0.55–1.5 eV (827–2254 nm) in high resolution (0.01 eV) steps at three angles of incidence (60°, 65°, and 70°). The AutoRetarder™ and isotropic and depolarization functions were active and the ellipsometer was initialized, aligned, and calibrated using a SiO_2/Si reference sample before each set of measurements. The beam diameter at the sample using alignment optics was approximately 1.5 mm. All measurements were taken at RT.

Refractive index and thickness data were calculated using J. A. Woollam WVASE32™ software and the Johs–Herzinger parametric semiconductor model.[31] A schematic representation of the model for the series 1 and 2 samples on silicon is shown in Fig. 4. Each sample was modeled as a series of parallel layers comprising the substrate, buffer layer, GaP nucleation layer, the $B_xGa_{(1-x)}As_yP_{(1-y)}$ layer of interest capped by an oxide/surface roughness layer. A similar model comprising a GaP substrate, the BGaAsP sample layer, and an oxide/surface roughness layer was applied for the series 3 samples.

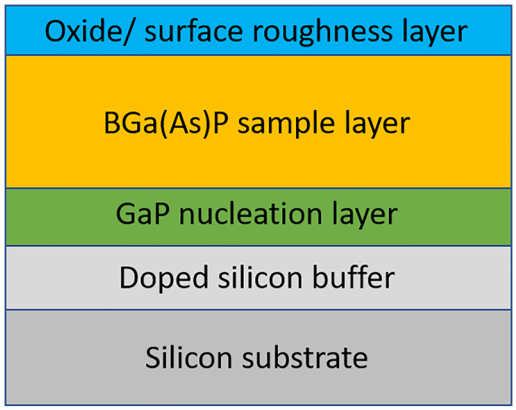

FIG. 4. Schematic cross section of the ellipsometry layer model for data fitting.

It has been assumed that all interfaces are sharp boundaries with no intermixing or roughness between layers and that optical constants are homogeneous. Scanning transmission electron microscope (STEM) investigations found no evidence of interdiffusion between layers and STEM and HR-XRD studies have not identified any signs of inhomogeneity.

The fewer the number of unknown material properties, the more accurate the model will be for determination of the optical parameters of the BGa(As)P layers. However, it is not possible to simply use dispersion functions from other studies for the silicon buffer or GaP layers, because the buffer layers are heavily doped and the GaP layer is under compressive strain due to its lattice mismatch with silicon, both of which alter their optical properties. For series 1 and 2, the optical constants for the doped silicon buffer layers on the silicon substrate were determined from samples A and G by applying a model comprising library values for the substrate, the nominal buffer layer thickness, and an upper oxide/ surface roughness layer. The GaP layer optical constants were then determined from samples B and H using the parameters from A and G above for the silicon substrate and buffer combination, the HR-XRD measured GaP layer thickness and an oxide/surface roughness layer. The modeled GaP on silicon layer optical parameters were then fixed for the ongoing BGa(As)P layer analysis, with the GaP thickness increased by the additional 4 nm growth to 32 nm. The optical properties of the GaP substrate (O) were measured and used as a constant base for the BGa(As)P layer analysis for series 3 samples.

The ellipsometric model parameters were determined layer by layer from the substrate upwards with each layer providing valuable data for device waveguide design. The model parameters for the strained GaP nucleation layer were adapted from a starting point of the J. A. Woollam WVASE32™ GaP_p parametric semiconductor library model[30] [referred to as *GaP parametric from UNL* (unpublished)]. The GaP nucleation layer parameters were then used as the starting point for determining the BGaP and BGaAsP model parameters. This consistent approach is important to ensure that the trends observed are a feature of differences in the physical properties of the materials rather than the possibility of variations in the methodology.

The experiments and analysis were carried out in the following order:

1. SE scans of each of the samples to measure ψ and Δ data as a function of wavelength (photon energy).
2. Creation of layer-by-layer parametric semiconductor models for each sample to fit the experimental ψ and Δ data.
3. Extraction of refractive index dispersion data points from the models for each sample.
4. Calculation of strain relaxed refractive index data points by applying the Lorentz–Lorenz equation Eq. (3).
5. Determination of strain relaxed Cauchy coefficients [Eq. (5)] as a function of boron and arsenic fractions.
6. Calculation of the strained refractive index variation with photon energy as a function of boron and arsenic fractions by applying the Cauchy model and Lorentz–Lorenz equation.

These data are illustrated as a surface between the sample dispersion curves allowing extrapolation to non-sample alloy fractions.

V. RESULTS AND DISCUSSION

A. Ellipsometric data

Figures 5(a) and 5(b) show examples of the experimentally measured (solid lines) and best fit model (dashed lines) ellipsometric parameters ψ and Δ for samples B (GaP on-silicon) and F (B = 6.6, As = 17%). Data for a single angle of incidence (65°) are shown for clarity. The oscillation features in Fig. 5(b) are due to thin film interference due to light reflected from the BGaAsP/GaP interface, which indicates that the BGaAsP layer is transparent, and that the real part of the refractive index of the GaP layer is lower than that of the BGaAsP layer in this range. This transparency feature was observed in all of the BGaP and BGaAsP samples. The thickness of the upper layer affects the number of oscillations and the refractive index difference between the layers affects their amplitude (and number). Oscillations are suppressed when the material becomes absorbing. There are no oscillation features for the GaP on-silicon sample because the silicon substrate is of a higher refractive index. It can be seen that there are no sharp critical point absorption features below ~2.3 eV.

B. Refractive index and strain

An important finding and consideration in our investigation has been the influence of strain on the refractive index measurements. As discussed earlier, we are interested in BGaP and BGaAsP alloy fractions, which are lattice matched to silicon at a growth temperature of 575 °C. Due to differences in their thermal expansion coefficients compared to silicon, these alloys become strained as they cool to RT. The relaxed lattice constant of the epilayer a_L is different from the substrate lattice constant a_S. When a thin ($<h_c$) epilayer is grown on a much thicker substrate, the epilayer lattice constant becomes equal to that of the substrate. The resulting net in-plane strain in the epilayer is given by

$$e_{||} = \frac{(a_S - a_L)}{a_L}. \tag{2}$$

For compressive strain ($a_L > a_S$), $e_{||}$ is negative and for tensile strain ($a_L < a_S$) $e_{||}$ is positive. For our samples, the substrate lattice constant a_S corresponds to silicon for series 1 and 2 and GaP for series 3. The epilayer relaxed lattice constants a_L for our samples were calculated by the application of Vegard's law using the lattice constant values shown in Table II.

Strain is well known to induce shifts in the band edges of the conduction and valence bands in semiconductors. The influence of strain on refractive index due to the change in density is discussed in detail by Kao[34] and has been applied practically in the form of the Lorentz–Lorenz equation by Tran *et al.*[35] as

$$n' = n + \frac{(n^2 - 1)(n^2 + 2)}{6n} e_{||}, \tag{3}$$

where n is the unstrained refractive index, n' is the as-measured, strained refractive index, and $e_{||}$ is the in-plane strain given by Eq. (2). Equation (3) implies that refractive index is decreased by the application of compressive strain and increased by tensile strain. The Lorentz–Lorenz equation is valid in wavelength regions remote from absorption bands, where absorption can be neglected, and the refractive index is real.[36] The applicability of the Lorentz–Lorenz equation (3) was confirmed by measuring the strained refractive index n' of the GaP layers on silicon (samples B and H), calculating the unstrained refractive index n,

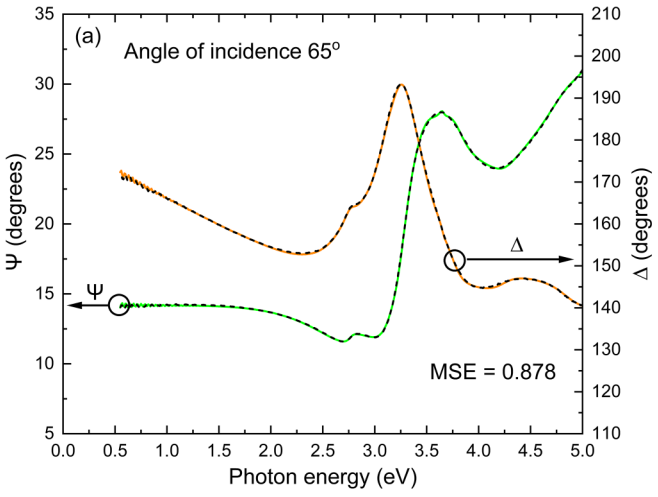

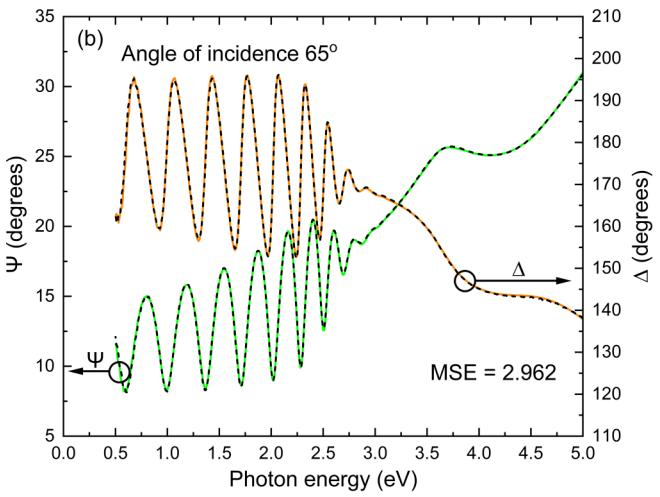

FIG. 5. Measured (solid lines) and modeled (dashed lines) ellipsometric parameters ψ and Δ at 65° angle of incidence. Sample B (GaP on-silicon) (a). Sample F (BGaAsP on GaP on-silicon) (b).

TABLE II. Material lattice constant values used in the calculation of in-plane strain.

Material	Lattice constant (Å)	Reference
Si	5.431 1	Okada and Tokumaru[5]
GaP	5.450 5	Vurgaftman *et al.*[6]
GaAs	5.653 25	Vurgaftman *et al.*[6]
BP	4.538	Huang *et al.*[32]
BAs	4.777	Hart and Zunger[33]

and comparing it with the measured bulk (unstrained) refractive index of the GaP substrate (sample O). The measured and calculated (unstrained) refractive indices agreed to within <0.003 in the range of 0.55–1.5 eV.

In this paper, we refer to "strained" refractive index as the *in situ* measured values of the epilayers relative to the specific substrate at room temperature and "strain corrected" values referring to the calculated unstrained values solved numerically using Eq. (3) and equivalent to the effective bulk material. The following results demonstrate the importance of taking substrate induced strain into consideration when applying refractive index data to waveguide design.

C. Refractive index measurements

Figures 6(a) and 6(b) show the measured refractive index and extinction coefficients of the GaP and BGa(As)P layers, over the full spectral operational range of the ellipsometer for a representative set of the on-silicon samples. The indicated critical point energies will be discussed in more detail later, however it can be seen that for the spectral range of interest, 0.55 eV–1.5 eV (shaded gray), there is no evidence of absorption or optical bandgap transitions confirming the applicability of Eq. (3).

The refractive index dependence, in the energy range of interest (0.55 eV–1.5 eV) on boron and arsenic fractions for the series 1 and 2, on-silicon samples are shown in Fig. 7. Results for the on-GaP, series 3, samples are consistent but not shown here for clarity. The refractive index variation with boron and arsenic fractions is also shown at selected photon energies 0.8 eV (1550 nm), 1.13 eV (1097 nm), 1.3 eV (956 nm), and 1.5 eV (827 nm) corresponding to wavelengths of interest and extending either side of the expected operating range of the GaNAsP laser system.

Results for the BGaP samples are shown in Figs. 7(a) and 7(b). Figure 7(a) shows the refractive index dispersion curves and the increase in refractive index with increasing boron fraction at fixed photon energy. Figure 7(b) further illustrates the increasing refractive index with boron fraction for the as-measured (strained) samples (solid circle data points and connecting lines) at the selected photon energies.

The corresponding strain corrected data points are indicated in Fig. 7(b) by the open circles and dashed connecting lines. From this, it can be seen that BGaP samples with layers, grown lattice matched with a boron fraction of ~3% at the growth temperature, are under tensile strain at RT which increases their refractive index. The compressive strain, for samples with boron fractions <2% at RT, causes a reduction in refractive index. The overall increase in refractive index due to boron incorporation up to 4.3% is ~0.04 and the flat strain corrected curves indicates that the change in refractive index is due to the effect of boron incorporation on the strain. This is an important finding, adding boron alone (up to 4.3%) to GaP has little effect on the refractive index of the bulk material, i.e., composition itself has little influence. However, the strain induced lattice distortion does impact the refractive index.

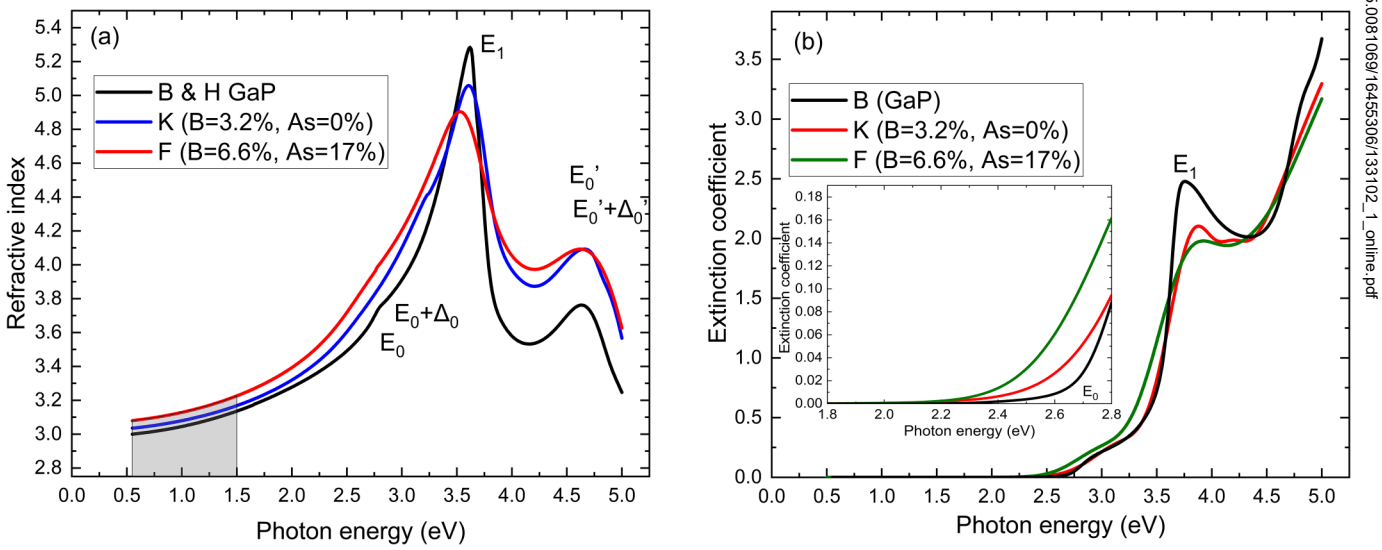

FIG. 6. Full spectral range refractive index (a) and extinction coefficient (with inset detail) (b) of GaP, BGaP and BGaAsP layers for selected on-silicon samples showing critical point energies.

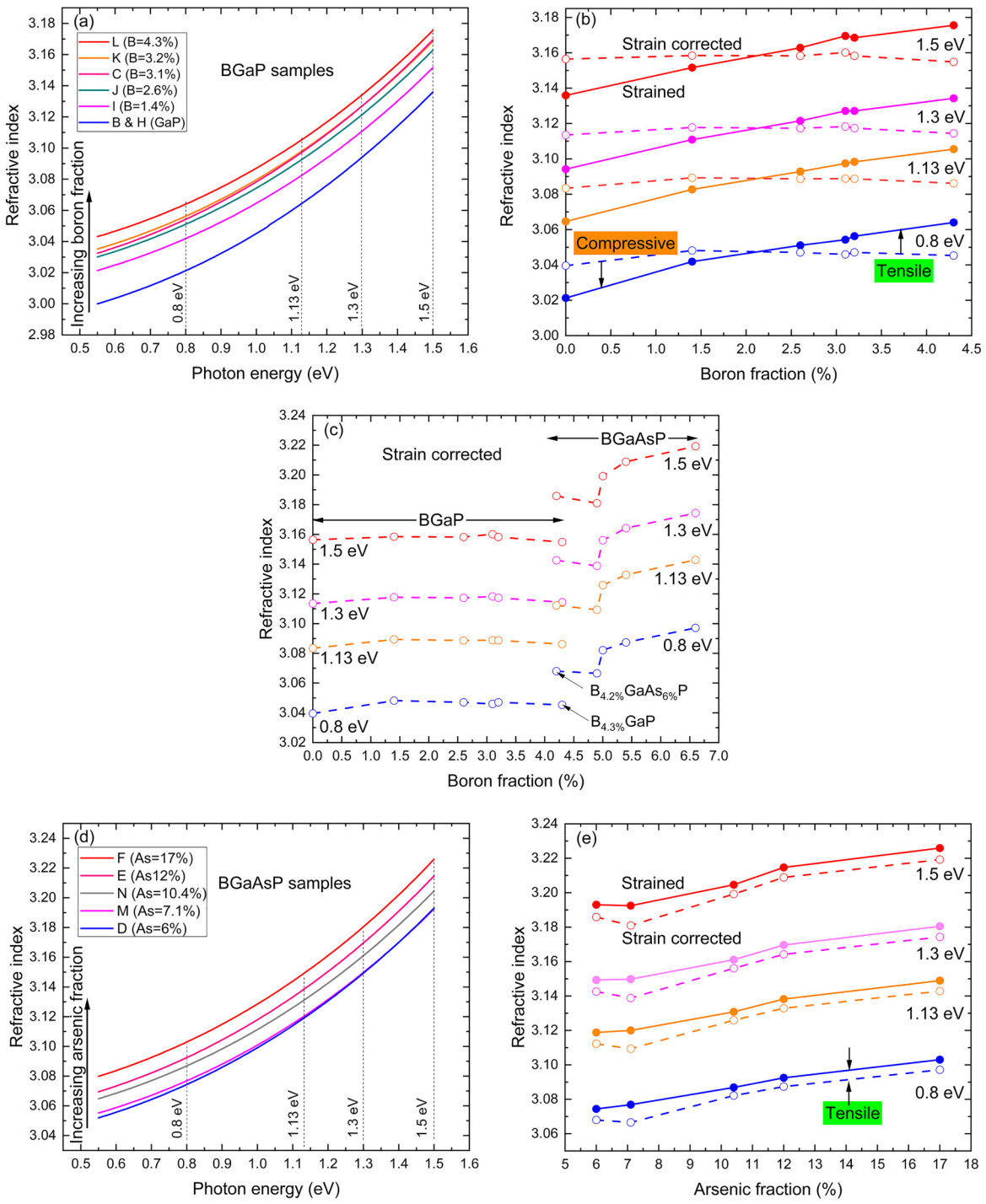

FIG. 7. Refractive index dispersion for BGaP on-silicon samples showing increasing refractive index with boron content (a). Strained and strain corrected refractive index of BGaP on-silicon samples showing refractive index change due to boron induced strain (b). Strain corrected refractive index of BGaP and BGaAsP on-silicon samples showing a stepwise increase due to introduction of arsenic (c). Refractive index dispersion for BGaAsP on-silicon samples showing increasing refractive index with arsenic content (d). Strained and strain corrected refractive index of BGaAsP on-silicon samples with arsenic content demonstrating refractive index increase due to tensile strain (e).

Figure 7(c) shows the strain corrected refractive index variation with boron fraction for the BGaP samples compared to the BGaAsP samples at the selected photon energies. On the left hand side, we see the flat strain corrected behavior of the BGaP samples, and on the right hand side, there is a stepwise increase in refractive index at the point where arsenic is included in the samples followed by a continuing increase in refractive index with increasing boron and arsenic content. The stepwise increase corresponds to the difference in refractive index between BGaP sample L with a boron fraction of 4.3% and BGaAsP sample D with a similar boron fraction of 4.2% and an arsenic fraction of 6%. These two sample points are indicated in Fig. 7(c) by the arrows either side of the discontinuity in the 0.8 eV data set. The refractive index of the arsenic-containing layer is ~0.03 higher than the similar boron only sample. The implication is that the increase in refractive index of the bulk material with arsenic fraction is related to the change in composition.

Figure 7(d) shows the refractive index dispersion curves and the increasing refractive index with increasing arsenic fraction (at fixed photon energy) for the BGaAsP samples. Figure 7(e) shows the as-measured (strained) and strain corrected refractive index variation with arsenic fraction for the BGaAsP samples at the selected wavelengths. There is a small and uniform difference in refractive index at RT due to tensile strain since all of these samples were lattice matched to silicon at the growth temperature. The as-measured and strain corrected refractive index increases by ~0.03 with increasing arsenic fraction from 6% to 17%.

For the boron and arsenic fractions considered, we can conclude that the inclusion of boron increases refractive index through the mechanism of strain while, for close to lattice matched (unstrained) combinations of boron and arsenic, the refractive index increases with increasing arsenic fraction.

In the context of the design of GaNAsP QW lasers grown on GaP/Si substrates, the BGaP cladding layer is always grown lattice matched to silicon at the growth temperature with a boron fraction of ~3%. The strained refractive index at the design or lasing photon energy (wavelength) can be read off from the plot for sample C in Fig. 7(a), as can the refractive index for the strained GaP on silicon nucleation layer (samples B and H).

Figure 8 illustrates the refractive index contrast at RT between the materials grown lattice matched to silicon at the growth temperature. In the context of waveguide design, it can be seen that the refractive index of the BGaAsP layers is greater than the BGaP cladding layer with the contrast increasing with the addition of arsenic. It also shows (orange shaded area) the range of refractive indices that can be achieved with different lattice matched BGaAsP compositions up to an arsenic fraction of 17%.

For context, we also show the refractive index of the silicon substrate and the slightly lower index of the n-doped silicon buffer layers (gray shaded area). This raises an important consideration for future investigation. In semiconductor laser devices the cladding is p-doped on one side of the active region and n-doped on the other. Figure 8 demonstrates that n-doping reduces refractive index (compared to the undoped material), and this effect has been seen in other experimental investigations by the authors and may be attributed to the Moss-Burstein effect.[37,38] A reduction in the refractive index of the lattice matched BGaP cladding layer due to n-doping would reduce its refractive index contrast with the adjacent GaP barrier and nucleation layers, increase its contrast with the BGaAsP SCH layer and change the balance of refractive index with the p-doped side of the device, which would change the optical confinement characteristics.

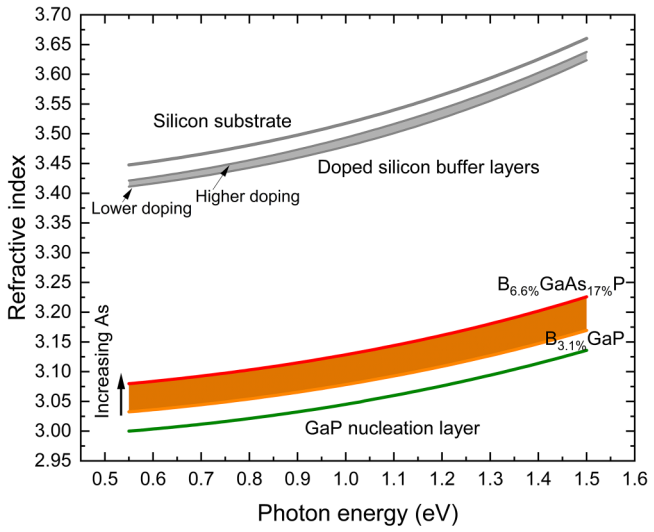

FIG. 8. Strained refractive index dispersion curves for the on-silicon samples showing the differences between the substrate, cladding, SCH, and barrier layers.

D. Refractive index model

In the case of the BGaAsP SCH layers, lattice matching at the growth temperature can be achieved with a range of boron and arsenic fraction combinations which may be, purposely, designed to be different on the n- and p-sides of the device. In order to investigate the optimum BGaAsP compositions for these devices, it is useful to be able to evaluate the refractive index at any intermediate composition, rather than just for the specific compositions of our samples, starting at the lattice matched BGaP composition of ~3% boron.

In a region of normal dispersion (no interband absorption), the variation in refractive index with wavelength for dielectrics and semiconductors can be described by the Cauchy expression

$$n(\lambda) = A + \frac{B}{\lambda^2} + \frac{C}{\lambda^4} + \ldots, \tag{4}$$

where A, B, and C are constants which are characteristic of a particular material. Alternatively, this may be written in terms of photon energy as

$$n(E_p) = P + QE_p^2 + RE_p^4 + \ldots, \tag{5}$$

with P, Q, and R as corresponding constants.

It can be seen from Figs. 6(a) and 6(b) that the range of 0.55–1.5 eV is a region of normal dispersion. The distinguishable critical point energies for GaP, taken from Table III, indicated in the figures can be seen to be well above the region of interest. Furthermore, it can be seen that the GaP indirect energy gaps at 2.26 and 2.63 eV are not distinguishable using SE.

TABLE III. GaP indirect energy gaps and critical point (CP) energies at 300 K (Adachi[39]).

E_g/CP	Energy (eV)
E_g^X	2.26
E_g^L	2.63
E_0	2.74
$E_0 + \Delta_0$	2.84
E_1	3.7
E_0	4.75
$E'_0 + \Delta'_0$	4.8

For BGaP with a lattice matched boron fraction of ~3%, the direct and indirect energy gaps have been determined to be ≥2 eV (Hossain *et al.*[18]) and, although the bandgap for BGaAsP is expected to decrease with increasing boron and arsenic fraction, the direct energy gap for our range of samples is also >2 eV (Volk and Stolz[17]). So, for the wavelength range of interest in this study, the refractive index is in the transparent region where absorption effects can be ignored. Parameters *P*, *Q*, and *R* for each sample layer were determined by fitting the measured, strain corrected, dispersion curves to Eq. (5). In order to create an empirical model, we need to understand how the dispersion coefficients *P*, *Q*, and *R* vary with boron and arsenic fraction. All three coefficients were found to increase with increasing boron and arsenic fractions as shown in Fig. 9. Note that although the dispersion of the Cauchy *Q* coefficient appears high, the calculated refractive index was found to be relatively insensitive to differences in the value of *Q* over its full dynamic range.

As demonstrated earlier, the increase in the strain corrected refractive index is due to the arsenic rather than the boron content and, for lattice matching to silicon at the growth temperature, there is a fixed relationship between the boron (x) and arsenic (y) fractions which was illustrated for the on-silicon samples in Fig. 3. This means that the strain corrected refractive index [Eq. (5)] can be expressed in terms of the photon energy and *P*, *Q*, and *R* as a function of the arsenic fraction only. The strained, on-silicon, refractive index model values can then be obtained by substituting the calculated values from Eq. (5) and Eq. (2) into Eq. (3). No higher order terms were required in Eq. (5) to achieve good fits to the experimental data.

The modeled surface representing the strained refractive index as a function of photon energy and arsenic fraction is shown in Fig. 10. The difference in refractive index between the modeled surface and the measured samples is typically better than ±0.003. The exception being for sample M (boron 4.9%, arsenic 7.1%) where the model over-predicts the refractive index by, at worst, 0.007 at the higher arsenic fraction and photon energy end. The sensitivity of the model was investigated and the maximum variation in the modeled *n*' due to the uncertainty in the curve fits for *P*, *Q*, and *R* was found to be ±0.007.

An alternative projection of the modeled data is shown in Fig. 11.

This illustrates the dynamic range of the refractive indices and enables a visual estimation of refractive index, for specific boron and arsenic lattice matched fractions, at photon energies between the selected values.

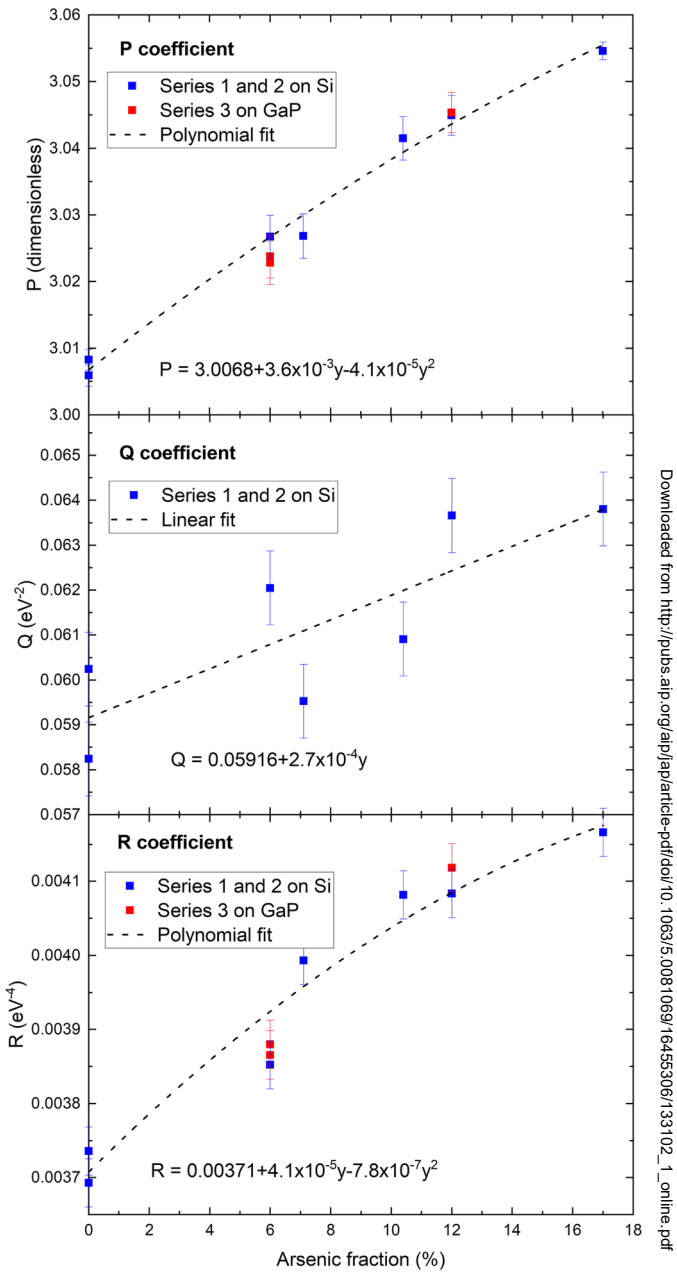

FIG. 9. Variation in the Cauchy parameters for the strain corrected empirical model as a function of arsenic fraction (y).

E. Waveguide applications

The model predicts that a refractive index contrast of ~0.05–0.07 can be achieved between lattice matched $B_{3.1\%}Ga_{96.9\%}P$ and $B_{7\%}Ga_{93\%}As_{19\%}P_{81\%}$ dependent on the selected wavelength.

It is of interest to compare this with more established material systems. Refractive index contrasts for $Al_xGa_{(1-x)}As$/GaAs measured

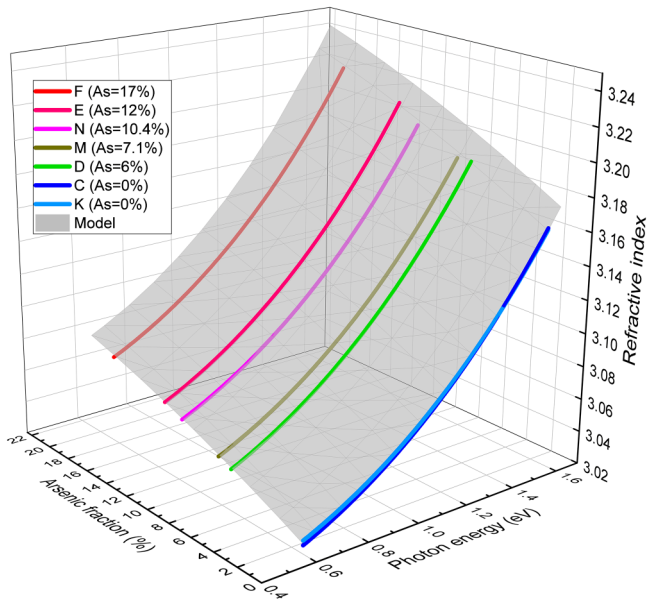

FIG. 10. Modeled (gray surface) and experimental (curves) strained refractive index as a function of photon energy and arsenic fraction for growth temperature lattice matched BGaP and BGaAsP layers on silicon.

using SE by Papatryfonos *et al.*[40] are ~0.2–0.3 for wavelengths in the range of 825–1550 nm. Similar contrasts have been measured and modeled by Seifert and Runge[41] using SE for the $In_{(1-x)}Ga_xAs_yP_{(1-y)}$/InP system in the same wavelength range. In practice, the contrasts

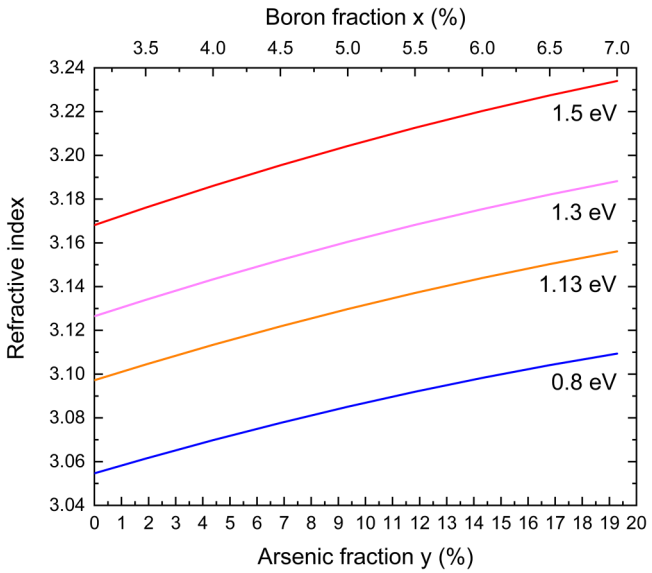

FIG. 11. Modeled refractive index variation for lattice matched boron and arsenic fractions at selected photon energies.

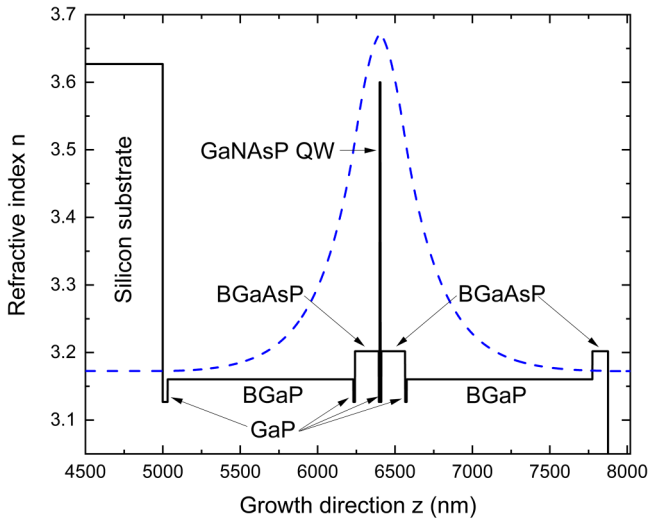

FIG. 12. Waveguide simulation showing the optical field distribution (blue dashed line—arbitrary units) at 850 nm (1.46 eV) confined within the device structure.

available are limited by the range of alloy fractions that meet device lattice matching and bandgap requirements.

A preliminary investigation suggests that the refractive index contrast is sufficient for BGaAsP waveguide applications of GaNAsP QW lasers on silicon. Figure 12 shows a waveguide simulation at 850 nm (1.46 eV), the primary wavelength for multimode fiber optical communication systems, for lattice matched BGaP cladding layers and $B_{5.5\%}GaAs_{11.5\%}P$ SCH and cap layers. The strained on-silicon refractive index values for silicon, GaP, and the boron containing alloys were as determined by SE or calculated from the model described above.

While not optimized, the selected cladding and SCH thicknesses and refractive index contrasts can be seen to provide good confinement of the optical field (blue dashed line) at this wavelength with an optical confinement factor of ~0.9%, for a 5.3 nm width single QW, which is relatively low compared, for example, to confinement factors of ~2% calculated for AlGaAs/GaAs devices by Hadjaj *et al.*[42] While an exact comparison is hard to obtain for InGaAsP/InP, using, for example, the data of Piprek *et al.*[43] and scaling for the same QW thickness, the optical confinement factor per QW is ~1%, which is very similar to the value calculated for our BGaP/BGaAsP waveguide.

Although the achievable contrast range is similar across our wavelength range, the degree of confinement of the mode within the core region will be greater at shorter wavelengths.[44] This means that there may be more scope for engineering and improving the waveguide properties at the lower wavelength end of the GaNAsP QW emission range.

VI. CONCLUSIONS

In this work, we used SE to analyze the refractive index dispersion of BGaP and BGaAsP layers epitaxially grown on silicon substrates as a function of boron and arsenic fractions. These layers are

of interest as cladding and SCH layers respectively in the development of GaNAsP QWs and an understanding of their optical properties is critical to laser waveguide design.

It was confirmed that strain due to lattice mismatch with the silicon substrate affects refractive index and, for the range of compositions of our samples an increase in boron fraction increases the refractive index through the mechanism of strain, while the increase in refractive index due to arsenic is independent of strain. The addition of boron up to 4.3% has only a weak effect on the refractive index of BGaP, which we speculate is band structure related. Since GaP and BP are both indirect bandgap semiconductors, the addition of boron to GaP alters its (indirect) band structure but the BGaP alloy remains indirect and as such has relatively little influence on the refractive index. This is in contrast to the addition of arsenic to GaP which moves it toward the direct bandgap GaAs, therefore having more of an influence on the refractive index. The method of analyzing the effect of strain can be more generally applied to the measurement of the optical properties of thin films on non-lattice matched substrates.

An empirical parametric dispersion model was developed, that takes account of the effects of strain, which can be used to calculate the refractive index of BGaP and BGaAsP layers lattice matched to silicon at a growth temperature of 575 °C as a function of boron and arsenic content. This provides data for waveguide modeling for a range of compositions without the need to grow new samples for analysis.

Preliminary simulation modeling, based on measured and modeled refractive indices, has confirmed that these novel boron containing materials can provide a viable waveguiding solution with further opportunity for optimization.

There is an opportunity to extend this investigation in the future using additional samples to review the impact of doping on refractive index. It is also recognized that lattice mismatch induced strain introduces anisotropy into the crystal layer. It is anticipated that the refractive index component in the growth direction (z) is dominant in the SE measurements, and important in terms of waveguiding. However, the components along the waveguide cavity (x and y), in the direction of the propagating field, should also be investigated in future work.

The results and methodology of this study are relevant to other applications using similar III-V and dilute nitride materials for integration on silicon.

ACKNOWLEDGMENTS

This work has been partly supported by EPSRC (UK) under Grant Nos. EP/N021037/1 and EP/V048732/1, a SEPnet PhD scholarship for D. A. Duffy and by the German Science Foundation (DFG) in the framework of the Graduate College 1782 "Functionalization of Semiconductors." The authors would like to acknowledge valuable conversations with Jianing Sun of the J. A. Woollam Company relating to ellipsometric modeling and Joseph Keddie and Zoe Bushell of the University of Surrey for their initial ellipsometer training.

AUTHOR DECLARATIONS

Conflict of Interest

The authors have no conflicts to disclose.

DATA AVAILABILITY

The data that support the findings of this study are available from the corresponding author upon reasonable request.

REFERENCES

[1]A. Y. Liu and J. Bowers, IEEE J. Sel. Top. Quantum Electron. **24**(6), 12 (2018).
[2]T. Suga, J. Bagdahn, H. Baumgart, C. Colinge, K. Hobart, and H. Moriceau, in *ECS Transactions* (IOP, 2009).
[3]R. Jones, P. Doussiere, J. B. Driscoll, W. Lin, H. Yu, Y. Akulova, T. Komljenovic, and J. E. Bowers, IEEE Nanotechnol. Mag. **13**, 17–26 (2019).
[4]A. Beyer, B. Haas, K. I. Gries, K. Werner, M. Luysberg, W. Stolz, and K. Volz, Appl. Phys. Lett. **103**, 032107 (2013).
[5]Y. Okada and Y. Tokumaru, J. Appl. Phys. **56**, 314–320 (1984).
[6]I. Vurgaftman, J. R. Meyer, and L. R. Ram-Mohan, J. Appl. Phys. **89**, 5815–5875 (2001).
[7]B. Kunert, S. Liebich, A. Beyer, R. Fritz, S. Zinnkann, K. Volz, and W. Stolz, J. Cryst. Growth **315**, 28–31 (2011).
[8]K. Volz, A. Beyer, W. Witte, J. Ohlmann, I. Nmeth, B. Kunert, and W. Stolz, J. Cryst. Growth **315**, 37–47 (2011).
[9]K. Volz, W. Stolz, and B. Kunert, in *22nd International Conference on Indium Phosphide Related Materials* (IEEE, 2010), p. 253.
[10]B. Kunert, K. Volz, J. Koch, and W. Stolz, Appl. Phys. Lett. **88**, 182108 (2006).
[11]B. Kunert, K. Volz, J. Koch, and W. Stolz, J. Cryst. Growth **298**, 121–125 (2007).
[12]N. Hossain, S. J. Sweeney, S. Rogowsky, R. Ostendorf, J. Wagner, S. Liebich, M. Zimprich, K. Volz, B. Kunert, and W. Stolz, Electron. Lett. **47**, 931 (2011).
[13]N. Hossain, S. R. Jin, S. J. Sweeney, S. Liebich, P. Ludewig, M. Zimprich, K. Volz, B. Kunert, and W. Stolz, in *IEEE International Conference on Group IV Photonics GFP* (IEEE, 2011), p. 148.
[14]S. Liebich, M. Zimprich, P. Ludewig, A. Beyer, K. Volz, W. Stolz, B. Kunert, N. Hossain, S. R. Jin, and S. J. Sweeney, in *Proceedings of 22nd IEEE International Semiconductors in Laser Conference* (IEEE, 2010), p. 143.
[15]S. Liebich, M. Zimprich, A. Beyer, C. Lange, D. J. Franzbach, S. Chatterjee, N. Hossain, S. J. Sweeney, K. Volz, B. Kunert, and W. Stolz, Appl. Phys. Lett. **99**, 071109 (2011).
[16]S. Rogowsky, M. Baeumler, M. Wolfer, L. Kirste, R. Ostendorf, J. Wagner, S. Liebich, W. Stolz, K. Volz, and B. Kunert, J. Appl. Phys. **109**, 053504 (2011).
[17]M. Volk and W. Stolz, J. Appl. Phys. **122**, 235702 (2017).
[18]N. Hossain, T. J. C. Hosea, S. J. Sweeney, S. Liebich, M. Zimprich, K. Volz, B. Kunert, and W. Stolz, J. Appl. Phys. **110**, 063101 (2011).
[19]G. W. Read, PhD thesis (University of Surrey, 2015).
[20]G. Leibiger, V. Gottschalch, B. Rheinländer, J. Šik, and M. Schubert, J. Appl. Phys. **89**, 4927–4938 (2001).
[21]J. A. Martin and M. Sanches, Rev. Mex. Fısica **61**, 245 (2015).
[22]H. S. Maczko, R. Kudrawiec, and M. Gladysiewicz, in *Proceedings of the International Conference on Numerical Simulation of Optoelectronic Devices, NUSOD 17* (IEEE, 2020).
[23]H. S. Maczko, R. Kudrawiec, and M. Gladysiewicz, Opt. Mater. Express **10**, 2962 (2020).
[24]H. S. Maczko, R. Kudrawiec, and M. Gladysiewicz, IEEE Photonics J. **12**, 1–13 (2020).
[25]L. N. Dvoretckaia, A. D. Bolshakov, A. M. Mozharov, M. S. Sobolev, D. A. Kirilenko, A. I. Baranov, V. Y. Mikhailovskii, V. V. Neplokh, I. A. Morozov, V. V. Fedorov, and I. S. Mukhin, Sol. Energy Mater. Sol. Cells **206**, 110282 (2020).
[26]S. Fan, Z. J. Yu, R. D. Hool, P. Dhingra, W. Weigand, M. Kim, E. D. Ratta, B. D. Li, Y. Sun, Z. C. Holman, and M. L. Lee, Cell Rep. Phys. Sci. **1**, 100208 (2020).
[27]S. Petznick, L. Ostheim, P. J. Klar, S. Liebich, K. Volz, and W. Stolz, Appl. Phys. Lett. **105**, 222105 (2014).
[28]Y. Zhang, Y. Ning, L. Zhang, J. Zhang, J. Zhang, Z. Wang, J. Zhang, Y. Zeng, and L. Wang, Opt. Express **19**, 12569 (2011).

[29]P. Ludewig, personal communication (NAsP III/V GmbH, Marburg, 2022).
[30]J. A. Woollam Co., Inc., *Guide to Using WVASE32: Spectroscopic Ellipsometry Data Acquisition and Analysis Software* (J. A. Woollam Co., Inc., Lincoln, NE, 2008).
[31]B. Johs, C. M. Herzinger, J. H. Dinan, A. Cornfeld, and J. D. Benson, Thin Solid Films **313–314**, 137–142 (1998).
[32]L. Huang, X. Wang, and B. Ao, J. Phys.: Condens. Matter **16**, 7829–7836 (2004).
[33]G. L. W. Hart and A. Zunger, Phys. Rev. B **62**, 13522–13537 (2000).
[34]K. C. Kao, *Dielectric Phenomena in Solids* (Elsevier Academic Press, San Diego, 2004).
[35]H. Tran, W. Du, S. A. Ghetmiri, A. Mosleh, G. Sun, R. A. Soref, J. Margetis, J. Tolle, B. Li, H. A. Naseem, and S. Q. Yu, J. Appl. Phys. **119**, 103106 (2016).
[36]R. S. Longhurst, *Geometrical and Physical Optics, Third* (Longman, London, 1976).
[37]T. S. Moss, Proc. Phys. Soc. Sect. B **67**, 775–782 (1954).
[38]E. Burstein, Phys. Rev. **93**, 632–633 (1954).
[39]S. Adachi, *Optical Constants of Crystalline and Amorphous Semiconductors*, 1st ed. (Springer, Boston, MA, 1999).
[40]K. Papatryfonos, T. Angelova, A. Brimont, B. Reid, S. Guldin, P. R. Smith, M. Tang, K. Li, A. J. Seeds, H. Liu, and D. R. Selviah, AIP Adv. **11**, 025327 (2021).
[41]S. Seifert and P. Runge, Opt. Mater. Express **6**, 629 (2016).
[42]F. Hadjaj, A. Belghachi, and A. Helmaoui, Int. J. Nanoelectron. Mater. **11**(1), 61 (2018).
[43]J. Piprek, P. Abraham, and J. E. Bowers, IEEE J. Quantum Electron. **36**, 366–374 (2000).
[44]P. E. N. Glytsis, *Introduction to Slab Dielectric Waveguides* (School of Electrical and Computer Engineering, National Technical University of Athens, 2020).